1 **Integration of 2D Hydraulic Model and High-Resolution LiDAR-derived**

2 **DEM for Floodplain Flow Modeling**

3 Dingtao Shen[a,b,c], Jiechen Wang[a,b,d], Xuejun Cheng[c], Yikang Rui[a,b], Song Ye[c]

4 [a]Jiangsu Provincial Key Laboratory of Geographic Information Science and Technology, Nanjing,

5 Jiangsu, China

6 [b]Department of Geographic Information Science, Nanjing University, Nanjing, Jiangsu, China

7 [c]Changjiang River Scientific Research Institute, Changjiang Water Resources Commission, Wuhan,

8 Hubei, China

9 [d]Jiangsu Center for Collaborative Innovation in Geographical Information Resource Development and

10 Application, Nanjing, Jiangsu, China

11

12 **Abstract:** The rapid progress of Light Detection And Ranging (LiDAR) technology has made acquirement

13 and application of high-resolution digital elevation model (DEM) data increasingly popular, especially

14 with regards to the study of floodplain flow modeling. High-resolution DEM data include many redundant

15 interpolation points, needs a high amount of calculation, and does not match the size of computational

16 mesh. These disadvantages are a common problem for floodplain flow modeling studies. two-dimensional

17 (2D) hydraulic modeling, a popular method of analyzing floodplain flow, offers high precision of elevation

18 parameterization for computational mesh while ignoring much micro-topographic information of the DEM

19 data itself. We offer a flood simulation method that integrates 2D hydraulic model results and

20 high-resolution DEM data, enabling the calculation of flood water levels in DEM grid cells through local

21 inverse distance weighted interpolation. To get rid of the false inundation areas during interpolation, it

22 employs the run-length encoding method to mark the inundated DEM grid cells and determine the real

23 inundation areas through the run-length boundary tracing technique, which solves the complicated problem

24 of the connectivity between DEM grid cells. We constructed a 2D hydraulic model for the Gongshuangcha

25 detention basin, a flood storage area of Dongting Lake, using our integrated method to simulate the

26 floodplain flow. The results demonstrate that this method can solve DEM associated problems efficiently

27   and simulate flooding processes with greater accuracy than DEM only simulations.

28

1 Introduction

31   Floodplain flow simulation is important for forecasting floods and assessing flood disasters. The typical

32   focus of simulation studies is to predict accurate flood inundation extent, depth and duration. In the field of

33   hydraulic calculation, to build a one-dimensional (1D) and two-dimensional (2D) hydraulic models is a

34   common method. In recent years, 2D hydraulic models are emerging as a standard for predicting flood

35   conditions, not only in the academic context but also in technical studies, replacing 1D approaches that,

36   despite their efficiency and the potential for their improvement in compound channels present conceptual

37   problems when applied to overbank flows(Gichamo et al., 2012; Costabile et al., 2015a). The preference

38   arises from their ability to more accurately predict complex out-of-bank flow patterns, overbank

39   depositional patterns, and stage-dependent position relative to 1D models (Abu-Aly et al., 2014).

40   Until the advent of survey technologies such as LiDAR, computational flood hydraulics was increasingly

41   limited by the data available to parameterize topographic boundary conditions rather than the sophistication

42   of model physics and numerical methods. New distributed data streams such as LiDAR, now pose the

43   opposite problem of how to use their vast information content optimally within a computationally

44   realizable context(Yu and Lane, 2006a; McMillan and Brasington, 2007). With the availability of high

45   resolution DEMs derived from LiDAR, 2D models can theoretically now be routinely parameterized to

46   represent considerable topographic complexity, even in urban areas where the potential exists to represent

47   flows at the scale of individual buildings. Many scholars have tried to apply high-resolution

48   LiDAR-derived DEM data to floodplain flow models and analyze the effects of different spatial DEM data

49 resolution on model calculations (Sanders, 2007; Moore , 2011; Sampson et al., 2012; Meesuk et al., 2015).

50 However, even where highly detailed topographic surveys are available, their direct use into high resolution

51 grids can be not feasible for large-scale flood inundation analysis (e.g., events involving both rural and

52 urban areas), both in terms of model preparation and computational burden(Dottori et al., 2013; Costabile

53 and Macchione, 2015b). Computational constraints on conventional finite element and volume codes

54 typically require model discretization at scales well below those achievable with LiDAR and are thus

55 unable to make optimal use of this emerging data stream(McMillan and Brasington, 2007). Traditional grid

56 coarsening approaches may reduce not only the computing demands, but also the accuracy of results due to

57 the loss of detailed information(Chen et al., 2012a). If DEM data only serves for the valuation assignments

58 of computational mesh nodes, then a lot of elevation point information is largely wasted(Marks and Bates,

59 2000). There is the need to use suitable procedures to obtain a reliable computational domain characterized

60 by a total number of elements feasible for a common computing machine.

61 In some early studies, the influence of sub-grid topography and obstructions such as vegetation and sparse

62 buildings are then treated by incorporating variability in constrained friction parameters(Horritt, 2000;

63 Mason et al., 2003; Bradbrook et al., 2004). This often results in friction values higher than empirically

64 derived values as the friction factor is attempting to parameterize friction on the sides of the flow as well as

65 bottom friction and incorporate the head loss associated with flow around structures(Fewtrell et al., 2008).

66 To raster-based 2D models, Yu developed a method for sub-grid-scale topographic representation with

67 explicit treatment of the effects of structural elements upon the floodplain upon both blockage and flux(Yu

68 and Lane, 2006b; Yu and Lane, 2011). In order to reduce the computational overhead of a raster model,

69 McMillan employed a porosity parameters to represent the effect of buildings and micro-relief on flow

70 pathways and floodplain storage(McMillan and Brasinton, 2007). According to Chen's researches, the

71   information from fine grid cells is extracted and simplified by using three parameters for a coarse-grid

72   resolution cell to reflect the cell's porosity(Chen et al., 2012a; Chen et al., 2012b). The area occupied by

73   buildings is expressed as the building coverage ratio(BCR) and the cross sections blocked by buildings on

74   the cell interfaces are described by the two conveyance reduction factors(CRFs). These sub-grid and

75   porosity parameterization methods enable efficient model applications at coarse spatial resolutions while

76   retaining information about the complex geometry of the built environment. However, while presenting

77   surface features, the flexibility of computational mesh of these raster models is not as good as that of

78   unstructured grid, such as irregular triangular elements. The unstructured grid allows one to modify the

79   density of the grid points accordingly to the topographic features and the expected hydraulic situations. Its

80   high degree of flexibility and adaptability provides an accurate geometrical description of the site even in

81   the presence of a significant topographical gradient or when the hydraulic variables are expected to change

82   very rapidly(Costabile and Macchione, 2015b). Nowadays, most hydrodynamic-numerical models are

83   solved using a finite element or finite volume approach on the basis of unstructured or hybrid

84   geometries(Mandlburger et al., 2009).

85   With the promotion of computer's processing capacity, hydraulic models directly based on meter-scale fine

86   grid have been applied(Schubert et al., 2008; Meesuk et al., 2015). In some researches, the resolution of

87   computational mesh even reached decimetric-scale (Fewtrell et al., 2011; Sampson et al., 2012)，which

88   improved the performance of 2D hydraulic models applying high-resolution DEM to some extent. Under

89   such fine scale，the topography under bridges and all the man-made features such as buildings and roads

90   can be presented accurately in computational mesh. Currently, how to deal with the influence of buildings

91   on water flow is a focus in relative researches. There are four main approaches(Schubert and Sanders,

92   2012):(1) The building-resistance (BR) method whereby a large resistance parameter value is assigned to

93   cells that fall within building footprints(Liang et al., 2007) or within developed parcels(Gallegos et al.,

94   2009; Gallien et al., 2011). (2) The building-block (BB) method whereby spatially distributed ground

95   elevation data are raised to the heights of rooftops(Brown et al., 2007, Schubert et al., 2008; Mandlburger et

96   al., 2009). (3) The building-hole (BH) method whereby the computational mesh is generated with holes

97   aligned with building walls, where free-slip wall boundary conditions are enforced(Schubert et al., 2008;

98   Costabile and Macchione, 2015b). (4) The building-porosity (BP) method where spatially distributed

99   parameters, including a porosity and a building drag coefficient, are introduced to model the impact of

100   buildings on flooding without resolving their exact geometries(Guinot, V., 2012, Sanders et al., 2008).

101   Unfortunately, the computational cost of 2D flood simulation at scales approaching 1 m is very high, and it

102   is not unusual to work with study areas of 100 km^2 or more (Sanders et al., 2010). According to Fewtrell's

103   research， when using an extremely efficient 2D code such as LISFLOOD-FP, the domain size is

104   approaching the limits of feasibility at 10 cm resolution, requiring 100 h on a high performance cluster. In

105   contrast, the ISIS-FAST simulation over the same domain could be run 750 times within the same

106   period(Fewtrell et al., 2011). Such models which directly employ a meter-scale high-resolution

107   computational mesh are limited by large study area. For example, the study area in Fewtrell's research

108   covers 0.11 km^2(Fewtrell et al., 2011), and the study area in Meesuk's research covers 0.4 km^2(Meesuk et

109   al., 2015). When the flood covers a relatively big extent, finer topographic data are typically re-sampled to

110   coarser meshes (Neal et al., 2009; Yu, 2010). The under-utilisation of high-resolution topographic data is

111   due, on one hand, to the exceptionally high computational requirements associated with fine-scale grids;

112   and on the other, to the small time steps required by this type of model in order to achieve computational

113   stability (Yu, 2010).

114   To improve the computational efficiency of hydraulic models, parallel technology has been employed in

115   calculating hydraulic models(Neal et al., 2010; Vacondio et al., 2014). In stand-alone application

116   environment, the efficiency of multi-core processors-based parallel computation can be several times

117   higher than that of single-core processors(Hervouet, 2000; Pau and Sanders, 2006). However, this

118   improvement on efficiency is still limited for enormous high-resolution DEM when applied to a large study

119   area(Chen et al., 2012a ; Costabile and Macchione, 2015b), though computer cluster-based parallel

120   computation is able to solve the problems caused by high-resolution DEM data applied in 2-D flood

121   simulation models(Sanders et al., 2010; Yu, 2010). One reason is parallel computation sets a higher request

122   of 2-D hydrologic model programming, because some complex procedures need to be taken into

123   consideration, such as data distribution, computer communication, model scheduling, etc. The other reason

124   is computer cluster-based parallel process has a high requirement on computer software and hardware

125   environment, so many relative researches are limited in laborites and are hard to promote its application.

126   The limitations of available computing resources, therefore, still restrict the applications when very detailed

127   information or risk-based analysis is required over large areas(Chen et al., 2012b). Actually, most of the

128   existing flood modeling packages are designed to work on medium size desktop machines, which does not

129   permit scaling to large size fine resolution domains. In general personal computers, efficient processing of

130   large amounts of DEM data and optimizing the precision of high-resolution vertical and horizontal

131   information is the key to efficient and accurate analysis of large-scale automatic floodplain flow models.

132   As a result, we put forward a new flood simulation method that integrates a 2D hydraulic model with

133   high-resolution DEM data. Starting with high-resolution DEM data, we constructed a comparatively coarse

134   computational mesh and then constructed a 2D hydraulic model. The results of the 2D hydraulic model

135   were overlaid with the high-resolution DEM data and the flood depth in DEM grid cells was calculated

136   using local inverse distance weighted interpolation. During the process of interpolation, there can be many

137 false flood areas in the DEM grid because parts of the grid cells are interpolated despite not being

138 inundated. To remove false-flooded areas, we marked all of the flooded areas using run-length encoding

139 and then got the real flood extent through run-length boundary tracing technology, a method that proved to

140 save much effort in verifying the connectivity between DEM grid cells. Lastly, we constructed a 2D

141 hydraulic model for the Gongshuangcha detention basin, which is a flood storage area of Dongting Lake,

142 and calculated the inundation extent and depth in different periods using our integrated method. By

143 analyzing and comparing the results, it proves that this method can enhance the accuracy and reliability of

144 floodplain flow modeling.

145 **2 Study Area and 2D Hydraulic Model**

146 **2.1 Study Area and DEM Dataset**

147 Dongting Lake (111°40′ ~113°10′ E, 28°30′ ~30°20′ N), with a total area of 18,780 km^2, is located in

148 the middle reaches of Yangtze River (Changjiang River, Figure 1). The districts through which the

149 Dongting Lake flows include Changde, Yiyang, Yueyang, Changsha, Xiangtan, and Zhuzhou in Hunan

150 Province as well as three cities in Jinzhou of Hubei Province. Dongting Lake is surrounded by mountains

151 on three sides and its fountainheads are varied and complicated. It is a centripetal water system fanning out

152 from the center. It only flows into the Yangtze River through Chenglingji of Yueyang (Figure 1).

153 (Insert figure 1 here)

154 In Changjiang River big flood occurred in 1860 and 1870, Ouchi and Songzi burst their banks. Flood

155 flowed into Dongting Lake with large quantity of sediment. Deposition of sediment has caused the rapid

156 growth of the bottomlands and highlands, and some of the watercourses, lakes and bottomlands have been

157 reclaimed. Since then, Dongting Lake has shrank from 4350 km^2 in 1949 to 2625 km^2 in 1995 (measured

158 by Changjiang Water Resources Commission in1995). The total of lake area and spillway area was less

159 than 4000 km^2, about 2/3 of its heyday. Nowadays, Dongting Lake is commonly divided into three parts:

East Dongting Lake, South Dongting Lake and West Dongting Lake, among which West Dongting Lake

has the largest water area.

Because of its special location and complex river network system, this area has been frequently prone to

flooding. Due to the heavy burden on the masses to deal with floods, lots of labor and money has been

spent on dike construction. In order to prevent floods, a total of 266 levees have been built around

Dongting Lake areas, and the total length of 5,812 km with the first rank 3,471 km and the second rank

1,509 km. Flooding events in this area have caused significant destruction. The cost of damages following

individual events in 1996 and 1998 was 15 and 8.9 billion Yuan, respectively. The pressure of preventing

flooding, and the associated damage, has been a major factor affecting healthy economic development and

improvement of living standards in Hunan province.

Flood storage and detention areas, which can guarantee the flood control and mitigate flood disaster in key

areas, are important components of river flood control system. Basin flood control planning requires to

develop regions where necessary conditions are satisfied into flood storage and detention areas, in order to

guarantee the flood control in key areas. Measuring overall, planned flood diversion, which guarantee the

safety in key areas while bringing loss to some other areas, is reasonable and necessary. At present, there

are 98 major flood storage and detention areas in China, which mainly located in middle-lower plain of

Changjiang River, Huanghe River, Huaihe River and Haihe River. Gongshuangcha detention basin, one of

the largest dry ponds in the Dongting Lake area, is located in the north of Yuanjiang county, facing South

Dongting Lake to the east and Chi Mountain to the west with water in between (Figure 2). In total, the

detention basin is 293 km^2 in storage area, 121.74 km in levee length, 33.65 m in storage height, has a

storage volume of 1.85×10^9 m^3, and is home to 160,000 inhabitants.

(Insert figure 2 here)

We have employed the airborne laser-measuring instrument HARRIER 86i, from German TopoSys

183 Company, for aerial photography of the Gongshuangcha detention basin from 1st to 8th October, 2010. The

184 digital camera we used was a Trimble Rollei Metric AIC Pro and the inertial navigation system was

185 Applanix POS/AV with a sampling frequency of 200Hz. The laser scanner was Riegl LMS-Q680i, with a

186 maximum pulse rate of 80KHz-400KHz and scanning angle of 45/60.

187 By processing the point cloud data, we derived a high-resolution DEM of the Gongshuangcha polder

188 detention basin (Figure 3). We checked DEM data quality on plane precision and elevation precision, and

189 the results showed that it could meet the application requirement. DEM plane position was checked by

190 GPS-RTK. After conversion parameters were set and control coordinates were confirmed, ground features'

191 plane coordinates, like corners of buildings, high-tension poles, telecom poles and road edges, were

192 measured. We checked 20 ground feature points, and plane position mean square error is 0.44m. DEM

193 elevation was checked by class 5 leveling. Using annexed leveling line or closed leveling line, we

194 calculated the elevation of check points and compared them with DTM and DEM. We checked 70 elevation

195 points, and elevation mean square error is 0.040m.

196 The spatial reference is the Gauss-Kruger projection coordinate system with Beijing 1954 datum, and the

197 elevation system is based on the 1985 national elevation standard, of which the lowest elevation is 4.55

198 meters and highest 45.87 meters. The general landscape shown in the DEM is flat, with much micro

199 topography information of levees, dikes and ridges retained (Figure 3).

200　　(Insert figure 3 here)

201 **2.2 2D Hydraulic Model**

202 In 2008, the Changjiang Water Resources Commission approved a report on the Comprehensive Treatment

203 Planning of Dongting Lake Area (Changjiang Water Resources Commission, 2008). The report highlighted

204 the serious threat of floods, which cause a surplus water volume of $21.8\text{-}28 \times 10^9$ m^3, in the middle and

205 lower reaches of Yangtze River. It also stressed that the effects of the Three Gorges Project, which greatly

206   influences the conditions for incoming water and sediments, must be taken into consideration. Even though

207   the completion of Three Gorges, and Xiluodu and Xiangjiaba Dams on the Chin-sha River can enhance the

208   flood draining ability around Chenglingji (Figure 1), at the confluence of Dongting Lake and Yangtze River,

209   is the report emphasized the urgent need to construct a 10×10^9 m^3 of diversion storage zone around

210   Chenglingji.

211   According to the Report on the Feasibility of the Flood Control Project of Qianliang Lake, Gongshuangcha

212   and East Datong Lake of Dongting Lake Areas (Ministry of Water Resources of China, 2009), flood waters

213   from events in 1954, 1966 and 1998, in Chenglingji could have been restricted to safely manageable levels

214   if local detention basins were set up to divert 8,000-12,000 m^3/s of rising waters. For the 1954 flood event,

215   the report shows that the maximum diversion should have been set at 10,000m^3/s, with Qianliang Lake

216   detention basin contributing 4,180m^3/s, Gongshuangcha detention basin 3,630m^3/s, and Datong Lake

217   detention basin 2,190m^3/s, with the corresponding water levels for the dikes set at 33.06m, 33.10m and

218   33.07m.

219   According to the standard design of the Gongshuangcha detention basin diversion, we simulated flood flow

220   using a mode controlled by sluice behavior. The resulting hydrograph acted as the input parameter, with

221   flood flow into the sluice conditioned as follows: when water level (H) was below 31.63m, the flow volume

222   into the sluice was 3,630m^3/s; when H was 31.63-32.60m, flow volume was 3,050 m^3/s; when H was

223   32.60-33.65m, another flow diversion exit was opened.

224   The flood routing model employed 2D unsteady shallow water equations to describe the water flow, used

225   FVM and Riemann approximate solvers to solve the coupled equations, and simulated flood routing inside

226   the detention basin. We used non-structural discrete mesh to represent the computational zone based on the

227   landscape of the area and the location of water conservancy projects. Then to make ensure accurate

228   conservation, we used FVM to decide bulk, momentum and the equilibrium of density for each mesh

229   element in different periods. To ensure precision, we used Riemann approximate solver to calculate the

230   bulk and normal numerical flux of the momentum between the mesh elements. The model solves the

231   equations through FVM discretions and converting 2D problems into series of 1D problems with the help

232   of the coordinate rotation of fluxes. The basic principles are as follows.

233   (1) Basic Control Equation. The Vector Expression of Conservative 2D Shallow Water Equation:

234
$$\frac{\partial q}{\partial t} + \frac{\partial f(q)}{\partial x} + \frac{\partial g(q)}{\partial y} = b(q) \qquad (1)$$

235   In this expression the conservative vector $q = [h, hu, hv]$T, the flux vector of X-direction $f(q) = [hu,$

236    $hu^2+gh^2/2, huv]$T, and the flux vector of Y-direction $g(q) = [hv, huv, hv^2+gh^2/2]$T. h is height, u and v

237   correspondingly mean the average uniform flux of X- and Y- directions, g is the gravity and the source term

238    $b(q)$ is:

239    $$b(q) = [q_w, gh(s_{0x} - s_{fx}) + q_w u, gh(s_{0y} - s_{fy})] \qquad (2)$$

240   In this expression, s_{0x} and s_{fx} are the river slope and friction slope on X-direction; s_{0y} and s_{fy} are the river

241   slope and friction slope on Y-direction; q_w is the net depth of water in each time unit. The friction slope

242   could be calculated through Manning Formula.

243   (2) The Discretization of Equations. Calculate basic FVM equation through discretization on any unit of Ω

244   by divergence principle.

245    $$\iint_{\Omega} q_t d\omega = -\int_{\partial \Omega} F(q) \cdot ndL + \iint_{\Omega} b(q)d\omega \qquad (3)$$

246   In this expression, n is the normal numerical flux outside of unit $\partial\Omega$, $d\omega$ and dL are surface integration and

247   line integration, and $F(q)$ n is the normal numerical flux, where $F(q) = [f(q), g(q)]^T$. These equations

248   demonstrate that the solution could convert 2D problems into series of local 1D problems.

249   (3) Boundary Condition. The model sets five kinds of flow boundaries: earth boundary, the outer boundary

250   of slow and rushing flow, the inner boundary, flowing boundary of no-water and water exchange unit and

251   tributary boundary of wetland.

252   (4) The solution to the equation. The equations, which are explicit finite schemes can be solved through

253   interactive method over time.

254   The computational mesh of the 2D hydraulic model of Gongshuangcha detention basin (Figure 4) is

255   constructed by a non-structural triangular mesh in which there are 83,378 triangles, each of whose side

256   length is between 100m-150m. The model mesh densifies the main levees with triangulars (each side length

257   is between 60m-80m). With the 1-m-resolution DEM data, we get the elevation value of the mesh node and

258   triangles centre points through nearest interpolation and make the value as the initial condition. The model

259   computes the water level of each triangular mesh's central point every 10 minutes. Finally, it simulates 50

260   periods' inundation processes (8 hours and 20 minutes in total).

261   (Insert figure 4 here)

262 **3 Methodology**

263 **3.1 Overview**

264   The inundation process is very hard to simulate because it varies over time. For each particular time, there

265   is a winding curved water surface. If we overlay the water surface calculated from a certain time with DEM

266   data, then the inundation area is where the water level is greater than topography elevation. As a result, the

267   key point of flood inundation simulation is to calculate water surface height. According to different

268   inundation models, there are three main computation methods: the flat-water model, 1D hydraulic model

269   and the 2D hydraulic model.

270   The flat-water model assumes that water level is a horizontal plane. In this method, flooding of cities or

271   coastal areas due to storms or rise of water level can be modeled relatively easily (Demirkesen et al, 2007;

272   Wang et al., 2002; John, 2001). Two common methods are used to decide the inundation extent from DEM:

273   the bathtub approach (Moorhead and Brinson 1995; Titus and Richman 2001) and the seeded region

274   growing approach (Poulter et al., 2008).

275   The Bathtub approach, also called "zero-side rule", does not take connectivity issue of DEM grid cells into

276   consideration. All the DEM grid cells whose elevation values are below floodwater level are regarded as

277   flooded areas, and the inundation extent consisted of DEM grid coverage, as expressed by Equation 4:

278   *Flood Extent = {cell:Z_{cell}<$Z_{water\ level}$, cell ∈Q}*   (4)

279   where Z_{cell} is the elevation value of DEM grid cell, $Z_{water\ level}$ fixes the level of floodwater, and Q is the

280   assemblage of DEM grid cells.

281   The seeded region growing approach considers DEM grid cell connectivity. The premise of the inundation

282   of DEM grid cells is that the elevation is below the floodwater level and also next to an inundated DEM

283   grid cell. This approach usually chooses some inundated DEM grid cells as seeds and then simulates the

284   flood diffusion by four-side or eight-side rule. The flood extent consists of the coverage of DEM grid, as

285   expressed by Equation 5:

286   *Flood Extent = {cell:Z_{cell}<$Z_{water\ level}$ ∧cell connect with point, cell ∈Q, point ∈P, P⊆Q}*   (5)

287   where *point* is a real inundated seeded grid cell, and *P* is the assemblage of inundated seeded grid cells

288   among the whole DEM grid.

289   1D hydraulic models can divide watercourses into cross sections and get the information of the water level

290   and flow of cross sections for unique time points. Because 1D hydraulic models do not involve detailed

291   topography information, it is hard to extract the parameters of inundation simply through calculating the

292   water level of cross sections. A good way to solve the problem is to calculate the actual depth of every

293   DEM grid cell and then decide the inundation extent (Tate et al., 1999). Similar to the flat-water model, this

294   model has to solve the connectivity issue during the process of performing interpolation on DEM grid cells

295   that are in-between cross sections. Interpolated cells that are not inundated cannot be connected with the

296   real inundated DEM grid cells of the watercourse. Previous work suggests that this issue can be solved

297   using methods such as geostatistical interpolation routines (March et al., 1990, Sorensen et al., 1996),

298   neighbourhood analysis (Jonge et al., 1996), and cost distance mapping (Werner, 2001).

299   2D hydraulic models, two common modeling computational meshes are regular tessellation and triangular

300   irregular net-TIN. Triangular irregular net-TIN is more popular has an advantage on showing the

301   topographic reliefs because it can improve the density of some areas of the triangular mesh to adjust to the

302   changes of terrain and provide a better realization of topographic relief (Casas et al., 2006). According to

303   different solutions of hydraulic computational equations, this model can get the water level of every mesh

304   node or the central point of mesh element at different time. As the hydraulic computation mesh is an

305   approximate expression of digital terrain, flood water level and inundation depth of each mesh unit can be

306   derived after calculating every water level value. Floodplain extent and inundation depth can be calculated

307   directly if there is low demand for result precision (Marks and Bates, 2000).

308   **3.2 Local Inverse Distance Weighted Interpolation**

309   With high-resolution DEM data, it is not precise to give the floodwater level for the whole DEM grid cells

310   in the mesh element directly because the actual elevation value of each cell in the DEM grid is different.

311   One reasonable way is to calculate water level of every DEM grid cell through spatial interpolation

312   technology like 1D hydraulic modeling. There are some common spatial discrete water level point-based

313   interpolation methods for flood water level including inverse distance weighted interpolation (Werner, 2001;

314   Moore, 2011) and linear interpolation(Apel et al, 2009). Some of the discrete points interpolation based on

315   natural neighbours, because of its comparatively better performance in evaluating terrain changes, also

316   have quite obvious advantages in flood level interpolation(Sibson, 1981; Belikov and Semenov, 1997;

317   Sukumar et al., 2001). Inverse distance weighted interpolation is a comparatively simple way to get the

318   spatial interpolation data, which can interpolate the value of unknown points with given the location and

319   value of known points. In a high-resolution DEM, we could get a water level value for each central point of

320   every DEM grid cell through interpolation, and compare the water level value with the elevation value of

321   DEM grid cell. If the water level value is higher than that of the DEM grid cell, it means this grid cell is

322   inundated. The inundation depth of the DEM grid cell is the water level value minus the grid cell elevation

323   value.

324   (Insert figure 5 here)

325   It is of high importance to choose computational mesh nodes as the known interpolated points for the water

326   level interpolation of DEM grid cells because it is improper to get all the nodes in a hydraulic model

327   involved in water level interpolation when tens or even hundreds of thousands computational mesh nodes

328   are involved. Figure 5 shows a non-structural modeling computation mesh (TIN). The computational water

329   level value of the model could be located on the central point of every triangle (as C1-C13 shows) or on the

330   node of the triangle (as P1-P12 shows) according to different solutions of the equation. For the cell located

331   at row I and column J of the DEM grid, we can decide the location of the cell by the spatial coordinate of

332   the central point. If a DEM grid cell (the black square) is inside $\triangle P1P2P3$, the following methods can be

333   used to choose the nodes of water level interpolation:

334   Firstly, get the coordinate and its water level value of the central point C13 of $\triangle P1P2P3$. Then search all

335   the triangles that share the nodes P1, P2 and P3 with $\triangle P1P2P3$, and calculate the coordinate of the central

336   points of these triangles (C1-C12) and their water level values. The Equation of water level of grid cell at

337   row I and column J is expressed as:

338 $$z(x) = \frac{\sum_{i=1}^{13} z(C_i) \times d_{ix}^{-2}}{\sum_{i=1}^{13} d_{ix}^{-2}} \qquad (6)$$

339 In this equation, x stands for the central point which is located at row I and column J of DEM grid, $z(C_i)$ is

340 the water level value of $NO.i$ known point, C is the central point of the triangle, and the distance between

341 each pair of $NO.i$ known point and grid node x is represented by d_{ix} raised to the power r, which is set as 2

342 for spatial data interpolation.

343 The method mentioned above can interpolate the inside of actual flood extent. As the water level elevation

344 of all the known points that are calculated in local areas are equal to the DEM grid cell elevation, DEM grid

345 cells that are not inundated can be decided without interpolating, which reduces the amount of calculation.

346 The method can also be employed for other kinds of computational grid, like a quadrilateral grid.

347 **3.3 Inundated Grid Cells Storing and Labelling**

348 Because much micro-topography information is retained in high-resolution LiDAR-derived DEM data,

349 many man-made surface features become a part of the DEM, like dams and trenches and the surfaces of

350 ponds that cannot be represented on some mid- or low-resolution DEM (Figure 6). Suppose that there is a

351 pond surrounded by levees in four-sides. Although the pond becomes inundated during the process of

352 interpolation, it is not actually flooded because the levees do not suffer from the flood. This is a typical

353 false inundation area. Another issue is ringed mountains, although the elevation of some areas among

354 mountains is lower than flood water level, these areas are not flooded because of the protection of the

355 mountains.

356 (Insert figure 6 here)

357 To solve the problem, calculated the actual flood extent based on the connectivity principle. However, some

358 judgment methods to solve the connectivity problem of flat-water and 1D hydraulic models are based on

359 the entire DEM. These methods cannot be applied to high-resolution DEM data because of the prohibitive

360 DEM size and the computation capability required. Using the seeded region growing method, a difficult

361 amount of data to process, 8.36GB (22,000 Rows × 51,000 Columns × 8 Bytes ≈ 8.36GB), stored in the

362 memory of a computer is required when dealing with the DEM data of our study area. On the other hand,

363 the seeded region growing method is a recursive algorithm with low efficiency of computation. Problems

364 like recursion might be too deep when dealing with a large amount of data and the stack of a computer is

365 overflowed to the extent that computation failures can occur. As a result, it is not an idealistic way to

366 employ such neighborhood analysis methods to solve DEM grid connectivity problems when facing a large

367 scale, high resolution, and an enormous amount of DEM data.

368 Due to a large amount of DEM data, which is hard to read for one time, it is better to divide the data into

369 strips to read. As Figure 7 shows, DEM data is divided into 5 strips spatially with each being read at one

370 time. The results of water level interpolations are concurrently stored on a raster file with a null value grid

371 equal to the source DEM data. Every time individual strip water level is interpolated, the result is stored on

372 a corresponding raster file. To process large volumes of DEM data, the memory that has been taken up by

373 the previous strip is released before next data strip is read.

374   (Insert figure 7 here)

375 There are two states for every grid cell during DEM grid interpolation: un-inundated and

376 might-be-inundated. This is typical binary raster data. If we perform run-length compressed encoding to the

377 sequential might-be-inundated DEM grid cells in raster rows, we can mark all the might-be-inundated cells

378 and store them in memory. Run-length encoding is a typical compressed method for raster data (Chang et

379 al., 2006; He et al., 2011), which encodes the cells with same value in compression. Every run-length only

380 needs to mark the cells where it starts across where it ends, which reduces the storage of data remarkably.

381 Figure 7 shows the run-length compressed encoding of the might-be-inundated DEM grid cells. Area A in

382 blue is the real inundation extent where there are three islands. There is a false inundation area inside the

383 middle island. The following are the equations of run-length data and run-length list on the raster:

384 *Run Length Dataset= {RLList: RLList =(RowIndex, RLNum, RLS)}* (7)

385 *RLS = {RL:RL=(RLIndex, StartCol, EndCol)}* (8)

386 As Equation 9 shows, run-length data is mainly comprised of the RL Lists on every raster row. The list

387 means the run-lengths of current raster rows, on which there are RowIndex, RLNum and RLS. In Equation

388 10, RLS consists of all the run-lengths on one raster row, and each run-length carries its RLIndex, StartCol

389 and EndCol.

3.4 Connectivity Detection Principle

391 After finishing DEM grid water level interpolation and storage of run-length compressed encoding of

392 inundated cells, the connectivity issue of DEM grid cells can be solved by run-length boundary tracing

393 technology (Quek, 2000). To prove the connectivity of two inundated cells of DEM randomly, only the

394 judgment of connectivity of the corresponding run-lengths is needed. Both the right and left borders of a

395 run-length are traced vertically and horizontally. if the two run-lengths are connected, then their borders can

396 be traced to form a closed loop.

397   (Insert figure 8 here)

398 As Figure 8 shows, three inundated cells in a raster field are marked in purple. To prove the connectivity

399 between Inundated cell 1 and Inundated cell 3 the run-length of Inundated cell 1 (the first run-length on the

400 raster row) and Inundated cell 3 (the fourth run-length on the raster row) must be found. If these

401 run-lengths are connected the boundary trace from the left of the run-length of 1 (as is shown from the

402 graph) to the right of 3 as long as it is on the left of 1.

403 If the boundary trace from the left of the run-length of Inundated cell 1 meets the right of the run-length of

404 Inundated cell 3, then the cells can be connected. Likewise, if the run-length of 1 and the run-length of 2

18

405   cannot meet each other by boundary tracing, then they are not connected. Based on mutual exclusion, as

406   long as we know that 1 is the real inundation area, all the areas connected to 1 are real inundation areas, and

407   all the areas connected to 2 are false inundation areas. As a result, the run-lengths have already carried the

408   information of connectivity between inundation grid cells and the connectivity problem could be worked

409   out through boundary tracing. Compared with the seeded region growing method, this method only need

410   search along the run-length borders to prove the connectivity between cells, allowing for far faster

411   computation speed.

412   **3.5 False Inundation Area Exclusion**

413   Based on the method mentioned above, we can remove false inundation areas from run-length boundary

414   tracing and get the map of flood extent and depth. Figure 9-(1) shows the run-length boundary tracing and

415   flood extent, in which run-lengths is marked in red rectangles. DEM data only includes 25 raster rows, the

416   model computation mesh is only expressed by four triangles, and the run-lengths are simplified. The water

417   level value of the central point of the mesh element is calculated by model computation, so we can

418   calculate the flood extent by tracing the boundaries of the run-lengths, which can be searched on the central

419   points of the whole computational model elements.

420   (Insert figure 9 here)

421   Take Figure 9-(1) for example, the inundated central point of $\triangle ABC$ can be found on the first run-length

422   on the eleventh raster through its spatial coordinate. From the left of this run-length, the outer boundary of

423   flood extent can be traced (Figure 9-(1)) and from the right of this run-length, one of the inner boundaries

424   of flood extent can be traced (Figure 9-(2)). The outer boundary of the entire flood extent can be also traced

425   through boundary tracing of the run-length that can be searched from the central point of $\triangle CDE$ (the 9th

426   row). To avoid repetition of run-length tracing, and to mark real inundated run-lengths, it is important to set

427   two labels along two sides of the run-length to indicate whether a run-length has previously been traced.

428 Run-lengths are marked as traced once one of the sides is traced. Boundary tracing of the run-length where

429 the central point of $\triangle$CDE is located is not performed when the run-length of the central point of $\triangle$ABC

430 has been traced.

431 After boundary tracing through all the central points of the inundated computational mesh elements, some

432 of the run-lengths are only traced by one side, like rows 5-8 and 12-17 in Figure 9-(2). They are located at

433 the islands of the flood extent. Traverse through the run-lengths to search the islands of the flood extent.

434 Once one side of a run-length is traced while the other not, all the islands can be found by tracing from the

435 untraced side and performing boundary tracing (Figure 9-(3)). At this time, there are only two kinds of

436 run-length. One is that each side of the run-length is traced, and the other is that neither side of the

437 run-length is traced. The extent of untraced run-lengths shows false inundation areas. Therefore, the false

438 inundation extent can be automatically removed by boundary tracing. Meanwhile, flood extent and depth

439 can be interpolated automatically from the traced run-length (Figure 9-(4)).

440 **4 Results and Discussion**

441 **4.1 Flood Inundation Results**

442 According to the principle mentioned above, we get the 50 periods' flood extent and depth of

443 Gongshuangcha detention basin of Dongting Lake area. Figure 10 (NO.10, No.30 and NO.50 periods)

444 shows the comparison between the result from the 2D hydraulic model and the result of the method

445 mentioned above. The resolution of the 2D hydraulic model mesh is above 100 meter, whereas this method

446 mentioned above interpolates the water level through 1m high-resolution DEM. As a result, although the

447 whole flood extents differ little, the distributions of flood depth are very different from each other. The

448 maximum inundation depth calculated by our method is 70cm higher than that of the 2D hydraulic model.

449 (Insert figure 10 here)

450 Figure 11 shows the No.50 period of process of inundation and its regional enlarged view. Figure 11-(1) is

451   the high-resolution aerial remote sensing image taken by an airborne LiDAR system, whose spatial

452   resolution is 0.3m. From this image we can see the distribution of farmlands, roads, channels, levees and

453   houses clearly, among which the houses are constructed along rivers and levees. Figure 11-(2) and 11-(3)

454   are the 2D hydraulic model and our methods regional enlarged view of the inundation area. The mesh

455   resolution of a 2D hydraulic model is coarser compared with the geographic features of roads and houses,

456   so the result can only prove that the flood depth of that area is lower while the ponds on the left of the

457   image cannot be expressed. It also cannot show the flood condition of every house. However, with the help

458   of our method, important geographic features can be clearly expressed. From Figure11-(3) it is obvious that

459   not only the flood condition of channels, ponds and levees are clearly expressed, but also the difference of

460   flood depths between ridges of paddy fields. In Figure11-(3) there are three linear areas which are not

461   inundated. From Figure11-(4) we can tell that those are levee crests on which houses and roads are being

462   constructed.

463   (Insert figure 11 here)

464   **4.2 Inundation Area and Volume statistics**

465   We compare the flood extents calculated from the 2D hydraulic model and the method mentioned above for

466   50 different periods. In the 2D hydraulic model, the flood extent is calculated by adding up every inundated

467   triangle's area from the hydraulic computational mesh, while in the method of this paper, the flood extent is

468   calculated by summing every real inundated cell area based on of 1-m-resolution DEM data. It can be

469   expected that the flood extent calculated from the 2D hydraulic model is larger than that from the method

470   of this paper (Figure 12). The 2D hydraulic model cannot take the micro-topography information into full

471   consideration, and many details cannot be shown on the model computational mesh, like some secondary

472   levees, ponds and steep slopes. We get a smaller area result because we can get rid of the parts in the

473   computational mesh whose elevation values are higher than the interpolated water levels.

474   Among the 50 periods, the flood area calculated by a 2D hydraulic model surpasses that of our method by

475   5%-17%.The exceeding flood area is getting larger. In the 50th period, the flood area of the 2D hydraulic

476   model is 6 square kilometers larger than that of this paper's method.

477   (Insert figure 12 here)

478   As for the inundation volume, the result calculated by the 2D hydraulic model is smaller than that

479   calculated by our method (Figure 13). According to the previous graphs the maximum inundation depth and

480   the regional inundation depth calculated by our method are larger than the 2D hydraulic model, which

481   means that the whole digital topography could be higher if we employ model computational mesh to

482   express the topography directly. The difference of results is from 3% to 8%, and in the 50th time-period, the

483   inundation volume difference is $9.689 \times 10^6 \text{m}^3$.

484   (Insert figure 13 here)

485   **4.3 Discussion**

486   The precision of digital topography is a key factor for flood simulation and analysis. Spatial resolution and

487   Vertical precision are both important for mapping of flood extent and depth. Employing high-resolution

488   topography data can make up for the errors of a 2D hydraulic model.

489   With high-resolution topography data, flood simulation can be analyzed from the basis of topography to

490   geographic elements because some of the most important micro-topography information is accounted for

491   by digital topography data, especially that of levees, ponds and man-made architectures. Once we take the

492   factors from the flood extent and depth map into consideration, we can get the results with more precision.

493   However, a coin has two sides. With more man-made architectures using high-resolution digital topography,

494   new problems might occur because some false topography information might be involved. For example, the

495   airborne LiDAR point cloud data could not be distinguished from the data of channels, bridges over reaches

496   or viaducts over roads. The redundant information could affect the simulation and analysis of floodplain

497 flow model. To remove redundant information, much later treatments are needed and might complicate the

498 situation.

5 Conclusion

500 With the help of photogrammetry and remote sensing technology, we can survey the digital terrain of a

501 large scale of reaches with high precision. Problems like a loss of topography materials and lack of data

502 accuracy are being gradually solved, allowing for progressively greater precision for analysis and

503 assessment of flood disaster risks. The rapid development of LiDAR technology has especially promoted

504 the acquirement and update of digital terrain data and shown its great potential for relevant study and

505 application to flood disaster studies.

506 To employ LiDAR-derived DEM to simulate flood routing directly is not realistic because of the

507 complexity of calculation of a hydraulic model with a prohibitively high-resolution mesh. Thus, we need to

508 construct a relative coarse model mesh on the basis of high-resolution digital topography. However, lots of

509 micro-topography information of high-resolution DEM has been ignored when we deal with flood

510 parameters, which have direct relation to inundation extent and depth. As a result, this paper hopes to offer

511 a method, which integrates a 2D hydraulic model with high-resolution LiDAR-derived DEM to simulate

512 floodplain flow. This method can calculate the flood extent and depth with much more precision during

513 floodplain flow modeling. With this kind of digital topography and data of residential houses and public

514 infrastructure, the floods caused by different reasons can be analyzed in greater detail. These factors

515 demonstrate the great application potential of our method for predictive flood simulation and accurate

516 assessment of potential loss from flooding events.

523 **References：**

524 Abu-Aly, T.R., Pasternack G.B., Wyrick J.R., Barker R., Massa D., Johnson T., 2014. Effects of LiDAR-derived, spatially

525 distributed vegetation roughness on two-dimensional hydraulics in a gravel-cobble river at flows of 0.2 to 20 times bankfull,

526 Geomorphology, 206:468-482.

527 Apel, H., Aronica, G.T., Kreibich, H., Thieken, A.H.. Flood risk analyses-how detailed do we need to be?[J]. Natural Hazards,

528 2009,49(1), 79-98.

529 Belikov, V.V., Semenov, A.Y., 1997. New NonSibson Interpolation on Arbitrary System of Points in Euclidean Space.

530 Proceedings of 15th World Congress on Scientific Computation Modeling and Applied Mathematics. Berlin August 1997.

531 Belikov, V.V., Semenov, A.Y., 2000. Non-Sibsonian interpolation on arbitrary system of points in Euclidean space and

532 adaptive isolines generation, Applied Numerical Mathematics, 32:371-387.

533 Bradbrook, K.F., Lane, S.N., Waller, S.G., Bates, P.D., 2004. Two dimensional diffusion wave modelling of flood inundation

534 using a simplified channel representation, Journal of River Basin Management, 3:1-13.

535 Brown, J.D., Spencer, T., Moeller, I., 2007. Modeling storm surge flooding of an urban area with particular reference to

536 modeling uncertainties: a case study of Canvey Island, United Kingdom, Water Resources Research, 43:W06402.

537 Casas, A., Benito, G., Thorndycraft, V.R., Rico, M., 2006. The topographic data source of digital terrain models as a key

538 element in the accuracy of hydraulic flood modelling[J]. Earth Surfaces Processes and Landforms, 31(4), 444-456.

539 Chang, C.C., Lin, C.Y., Wang, Y.Z., 2006. New image steganographic methods using run-length approach[J]. Information

540 Science, 176(22), 3393-3408.

541   Chen, A.S., Evans, B., Djordjevic, S., Savic, D.A., 2012a. Multi-layered coarse grid modelling in 2D urban flood simulations,

542   Journal of Hydrology, 470-471:1-11.

543   Chen, A.S., Evans, B., Djordjevic, S., Savic, D.A., 2012b. A coarse-grid approach to representing building blockage effects in

544   2D urban flood modelling, Journal of Hydrology, 426:1-16.

545   Chen, J., Hill, A.A., Urbano, L.D., 2009. A GIS-based model for urban flood inundation[J]. Journal of Hydrology, 373,

546   184-192.

547   Costabile, P., Macchione, F., Natale, L., Petaccia, G., 2015a. Flood mapping using LIDAR DEM. Limitations of the 1-D

548   modeling highlighted by the 2-D approach[J]. Natural Hazards, 77(1):181-204.

549   Costabile, P., Macchione, F., 2015b. Enhancing river model set-up for 2-D dynamic flood modelling, Environmental

550   Modelling & Sftware, 67:89-107.

551   CWRC, 2008. Comprehensive Treatment Planning of Dongting Lake Area, Changjiang Water Resources Commission, China.

552   Demirkesen, A.C., Evrendilek, F., Berberoglu, S., Kilic, S., 2007. Coastal Flood Risk Analysis Using Landsat-7 ETM+

553   Imagery and SRTM DEM: A Case Study of Izmir, Turkey[J]. Environmental Monitoring and Assessment, 131(1-3), 293-300.

554   Dottori, F., Di Baldassarre, G., Todini, E., 2013. Detailed data is welcome, but with a pinch of salt: Accuracy, precision, and

555   uncertainty in flood inundation modeling, WATER RESOURCES RESEARCH, 49:6079-6085.

556   Fewtrell, T.J., Bates, P.D., Horrit, M., Hunter, N.M., 2008. Evaluating the effect of scale in flood inundation modelling in

557   urban environments, HYDROLOGICAL PROCESSES, 22:5107-5118.

558   Fewtrell, T.J., Duncan, A., Sampson, C.C., Neal, J.C., Bates, P.D., 2011. Benchmarking urban flood models of varying

559   complexity and scale using high resolution terrestrial LiDAR data[J]. Physics and Chemistry of the Earth, 36, 281-291.

560   Gallegos, H.A., Schubert, J.E., Sanders, B.F., 2009. Two-dimensional, high-resolution modeling of urban dam-break flooding:

561   a case study of Baldwin Hills, California, Advances in Water Resources, 32:1323-1325.

562   Gallien, T.W., Schubert, J.E., Sanders, B.F., 2011. Predicting tidal flooding of urbanized embayments: a modeling framework

563   and data requirements, Coastal Engineering, 58:567–77

564   Gichamo, T.Z., Popescu, I., Jonoski, A., Solomatine, D., 2012. River Cross-section extraction from the ASTER global DEM

565   for flood modeling[J]. Environmental Modelling & Software, 31, 37-46.

566   Guinot, V., 2012. Multiple porosity shallow water models for macroscopic modelling of urban floods. Advances in Water

567   Resources, 37:40-72.

568   He, Z., Sun, W., Lu, W., Lu, H., 2011. Digital image splicing detection based on approximate run length[J]. Pattern

569   Recognition Letters, 32(12), 1591-1597.

570   Hervouet, J., 2000. A high resolution 2-D dam-break model using parallelization. Hydrological Processes 14(13), 2211–2230.

571   Horritt, M.S., 2000. Calibration and validation of a 2-dimensional finite element flood flow model using satellite radar

572   imagery. Water Resources Research 36 (11), 3279–3291.

573   John Dobosiewicz, 2001. Application of Digital Elevation Models and Geographic Information Systems to Coastal Flood

574   Studies along the Shoreline of Raritan Bay, New Jersey[J]. Environmental Geoscience,8(1), 11-20.

575   Jonge, T. de, Kok, M., Hogeweg, M., 1996. Modelling floods and damage assessment using GIS, in HydroGIS96:

576   Application of Geographical Information Systems in Hydrology and Water Research. Management and Planning Proceedings

577   of the Vienna Conference, 4-1996, IAHS Publ, 235, 299-306.

578   Liang, D., Falconer, R.A., Lin, B., 2007. Coupling surface and subsurface flows in a depth averaged flood wave model,

579   Journal of Hydrology, 337(1-2):147-158.

580   Mandlburger, G., Hauer, C., Hofle, B., Habersack, H., Pfeifer, N., 2009. Optimisation of LiDAR derived terrain models for

581   river flow modelling, Hydrology and Earth System Sciences, 13:1453-1466.

582   March, C., Lessard, G, Gharbi, B.El.. Kriging technique for river flood representation, Journal of Hydraulic Research,

583   1990,28(5), 629-643.

584   Marks, K., Bates, P., 2000. Integration of high-resolution topographic data with floodplain flow models[J].

585   HYDROLOGICAL PROCESS, 14, 2109-2122.

586   Mason, D.C., Cobby, D.M., Horritt, M.S., Bates, P.D., 2003. Floodplain friction parameterization in two-dimensional river

587   flood models using vegetation heights derived from airborne scanning laser altimetry. Hydrological Processes 17 (9),

588   1711–1732.

589   McMillan, H.K., Brasington, J., 2007. Reduced complexity strategies for modelling urban floodplain inundation,

590   Geomorphology, 90:226-243.

591   Meesuk, V., Vojinovic, Z., Mynett, A.E., Abdullah, A.F., 2015. Urban flood modelling combining top-view LiDAR data with

592   ground-view SfM observations, Advances in Water Resources, 75:105-117.

593   Moore, M.R., 2011. Development of a high-resolution 1D/2D coupled flood simulation of Charles City, Iowa. MS (Master of

594   Science) thesis, University of Iowa, 49-68.

595   Moorhead, K.K., Brinson, M.M., 1995. Response of wetlands to rising sea level in the lower coastal plain of North

596   Carolina[J]. Ecological Applications, 5, 261-271.

597   MWR, 2009. Report on the Feasibility of the Flood Control Project of Qianliang Lake, Gongshuangcha and East Datong

598   Lake of Dongting Lake Areas, Ministry of Water Resources, China.

599   Neal., J.C., Bates, P.D., Fewtrell, T.J., Hunter, N.M., Wilson, M.D., 2009. Distributed whole city water level measurements

600   from the Carlisle 2005 urban flood event and comparison with hydraulic model simulations, Journal of Hydrology,

601   368:42-55.

602   Neal, J.C., Fewtrell, T.J., Bates, P.D., Wright, N.G., 2010. A comparison of three parallelisation methods for 2D flood

603   inundation models[J]. Environmental Modelling & Software, 25:398-411.

604   Pau, J.C., Sanders, B.F., 2006. Performance of parallel implementations of an explicit finite-volume shallow-water model[J].

605   Journal of Computing in Civil Engineering, 20 (2), 99–110.

606   Poulter, B., Halpin, P.N., 2008. Raster modelling of coastal flooding from sea-level rise[J]. International Journal of

607   Geographical Information Science, 22(2), 167-182.

608   Quek, F.K.H., 2000. An algorithm for the rapid computation of boundaries of run-length encoded regions[J]. Pattern

609   Recognition. 2000, 33(10), 1637-1649.

610   Sampson, C.C., Fewtrell, T.J., Duncan, A., Shaad, K., Horrit, M.S., Bates, P.D., 2012. Use of terrestrial laser data to drive

611   decimetric resolution urban inundation models, Advances in Water Resources, 14:1-17.

612   Sanders B.F., 2007. Evaluation of on-line DEMs for flood inundation modeling[J]. Advance in Water Resources, 30,

613   1831-1843.

614   Sanders, B.F., Schubert, J.E., Gallegos, H.A., 2008. Integral formulation of shallow-water equations with anisotropic porosity

615   for urban flood modeling, Journal of Hydrology, 362:19-38.

616   Sanders, B.F., Schubert, J.E., Detwiler, R.L., 2010. ParBreZo: A parallel, unstructured grid, Godunov-type, shallow-water

617   code for high-resolution flood inundation modeling at the regional scale. Advances in Water Resources, 33,1456-1467.

618   Schubert, J.E., Sanders, B.F., Smith, M.J., Wright, N.G., 2008. Unstructured mesh generation and landcover-based resistence

619   for hydrodynamic modeling of urban flooding, Advances in Water Resources, 31:1603-1621.

620   Schubert, J.E., Sanders, B.F., 2012. Building treatments for urban flood inundation models and implications for predictive

621   skill and modeling efficiency, Advances in Water Resources, 41:49-64.

622   Schumann, G., Matgen, P., Cutler, M.E.J., Black, A., Hoffmann, L., Pfister, L., 2008. Comparison of remotely sensed water

623   stages from LiDAR, topographic contours and SRTM[J]. ISPRS Journal of Photogrammetry & Remote Sensing, 63, 283-296.

624   Sibson, R., 1981. A brief description of the natural neighbor interpolant. In: Interpreting Multivariate Data, John Wiley &

625   Sons, Chicester, 21-36.

626   Sorensen, H.R., Kjelds, J.T., Deckers, F., Waardenburg F., 1996. Application of GIS in hydrological and hydraulic modelling:

627   DLIS and MIKEⅡ-GIS, HydroGIS 96: Application of Geographical Information Systems in Hydrology and Water Res.

628   Management and Planning(Proceedings of the Vienna Conference, 4-1996, IAHS Publ. 235, 149-156.

629   Sukumar, N., Moran, B., Belikov, V.V., 2001. Natural neighbour Galerkin methods[J]. International Journal for Numerical

630   Methods In Engineering, 50:1-27.

631   Tate, E., Maidment, D. 1999. Floodplain mapping using HEC-RAS and ArcView GIS, CRWR Online Report 99-1, Center for

632   Research in Water Resources, University of Texas at Austin.

633   Titus, J.G., Richman, C., 2001. Maps of lands vulnerable to sea level rise: modeled elevations along the US Atlantic and Gulf

634   coasts. Climate Research, 18, 205-228.

635   Vacondio, R., Dal Palu, A., Mingnosa, P., 2014. GPU-enhanced Finite Volume Shallow Water solver for fast flood

636   simulations, Environmental Modelling & Software, 57:60-75.

637   Werner, M.G.F. , 2001. Impact of Grid Size in GIS Based Flood Extent Mapping Using a 1D Flow Model[J]. Phys. Chem.

638   Earth(B), 26(7-8), 517-522.

639   Wang, Y., Colby, J.D., Mulcahy, K.A., 2002. An Efficient method for mapping flood extent in a costal floodplain using

640   Landsat TM and DEM data[J]. International Journal of Remote Sensing, 23(18), 3681-3696.

641   Yu, D., Lane, S.N., 2006a. Urban fluvial flood modelling using a two-dimensional diffusion-wave treatment, part 1: mesh

642   resolution effects, HYDROLOGICAL PROCESSES, 20:1541-1565.

643   Yu, D., Lane, S.N., 2006b. Urban fluvial flood modelling using a two-dimensional diffusion-wave treatment, part 2:

644   development of a sub-grid-scale treatment, HYDROLOGICAL PROCESSES, 20:1541-1565.

645   Yu, D., 2010. Parallelization of a two-dimensional flood inundation model based on domain decomposition, Environmental

646   Modelling & Software, 25:935-945.

647   Yu, D., Lane, S.N., 2011. Interactions between subgrid-scale resolution, feature representation and grid-scale resolution in

648   flood inundation modelling, Hydrological Processes, 25(1): 36-53.

649   Zerger, A., 2002. Examining GIS decision utility for natural hazard risk modeling[J]. Environmental Modeling & Software[J].

650   17, 287-294.

651

652

670　　**Figures**

671

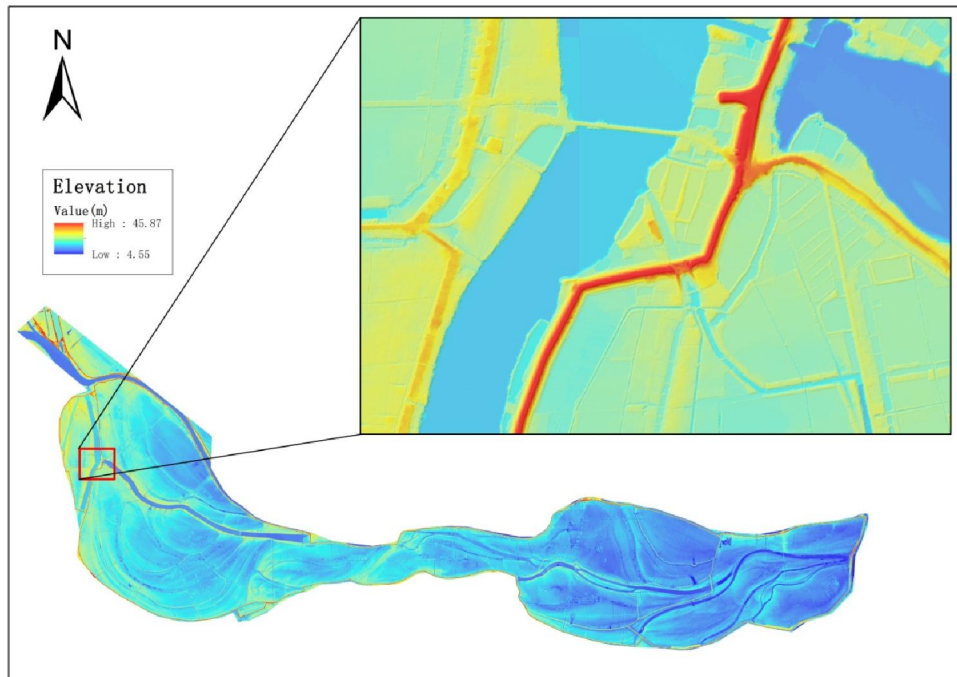672　　　　　　　　　Figure1. The location of Dongting Lake in Yangtze River Basin.

673

674　　　　　　　Figure2. The location of Gongshuangcha detention basin in Dongting Lake Area.
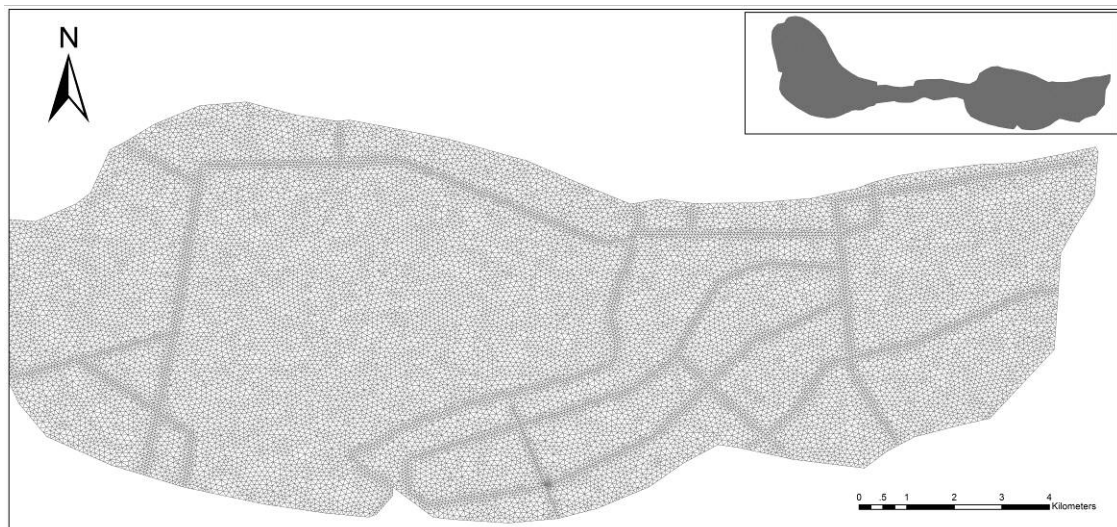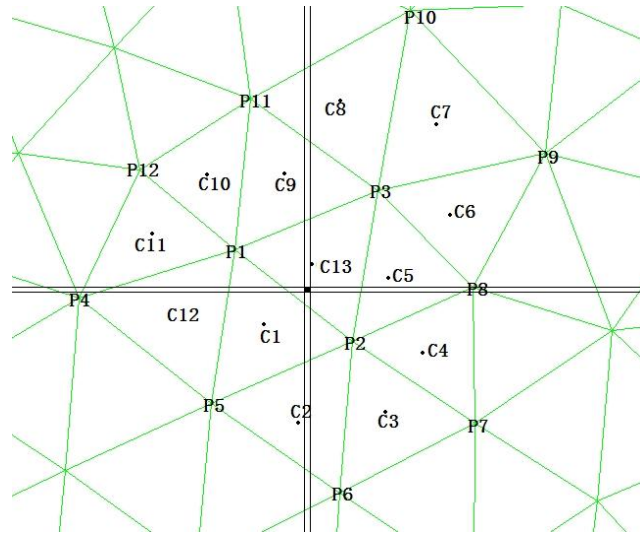
675
676   Figure 3. 1-m-resolution DEM data for the Gongshuangcha detention basin. Coverage shown is 50×20km,
677   Space resolution of 1m, DEM grid is 22,000 rows×51,000 columns, and file size is 4.18GB.
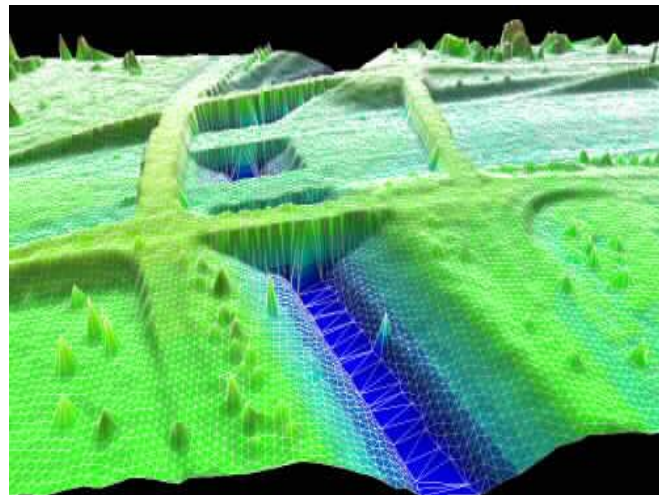

678
679   Figure 4 The 2D hydraulic model mesh of Gongshuangcha detention basin and its regional enlarged view.

680

681   Figure 5 The Scheme of Spatial Interpolation.

682

683   Figure 6 The Micro-topography Information of DEM.
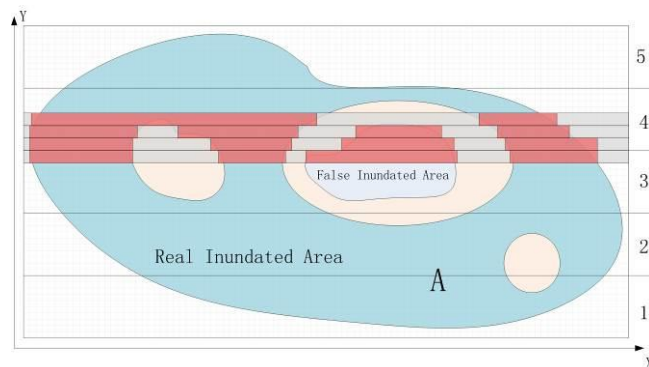
684

685   Figure 7 Run-length Compressed Encoding of DEM.

686
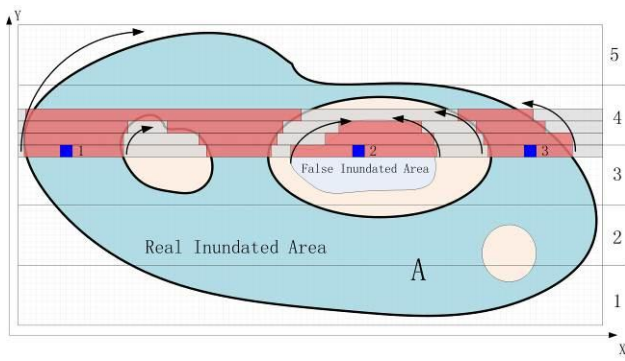
Figure 8 Connectivity Detection between DEM Grid Cells.

688

689
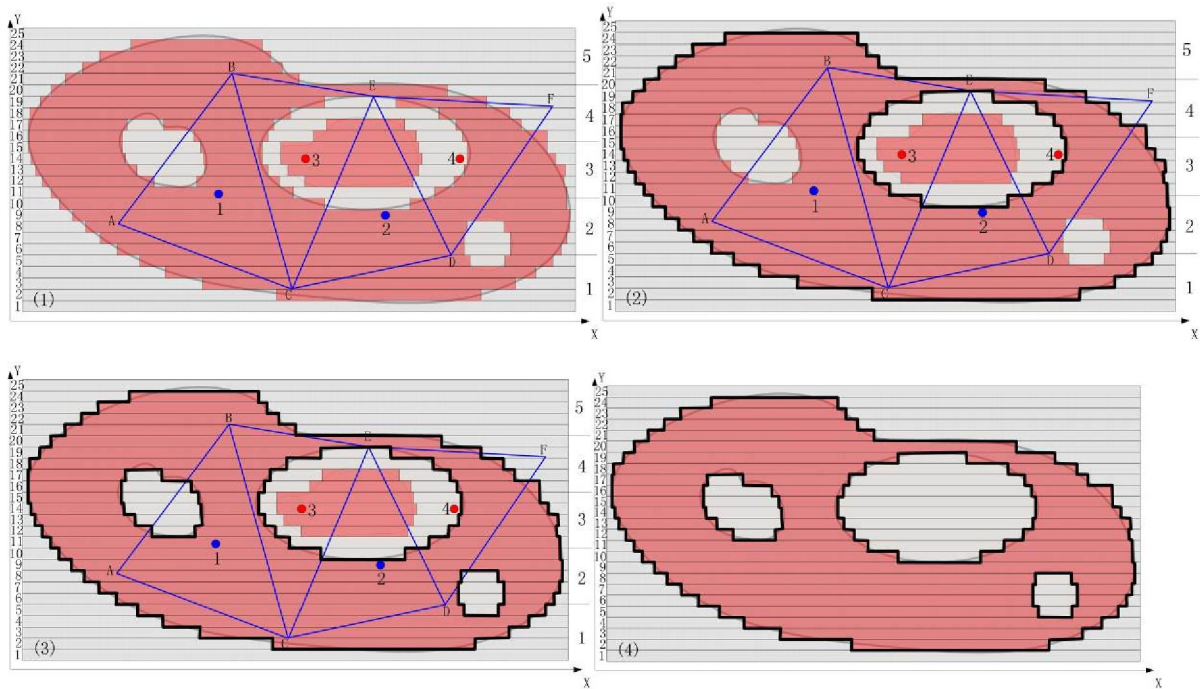
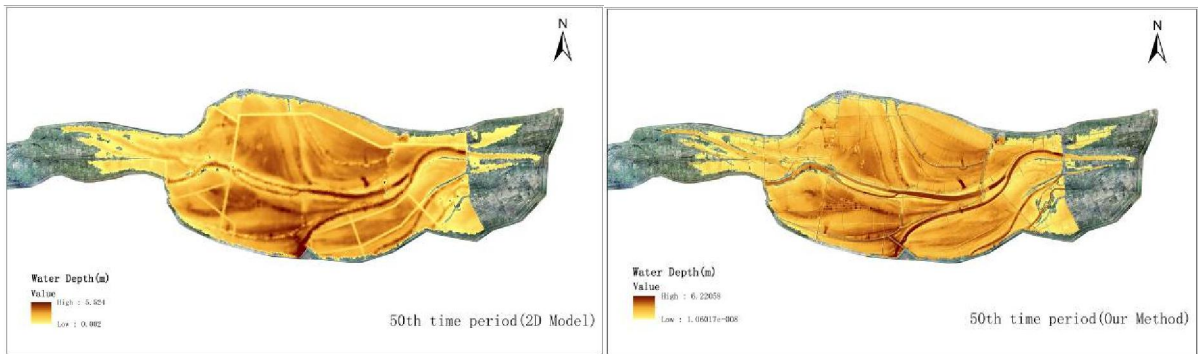Figure 9 The scheme of run-length boundary tracing and the derived flood extent.
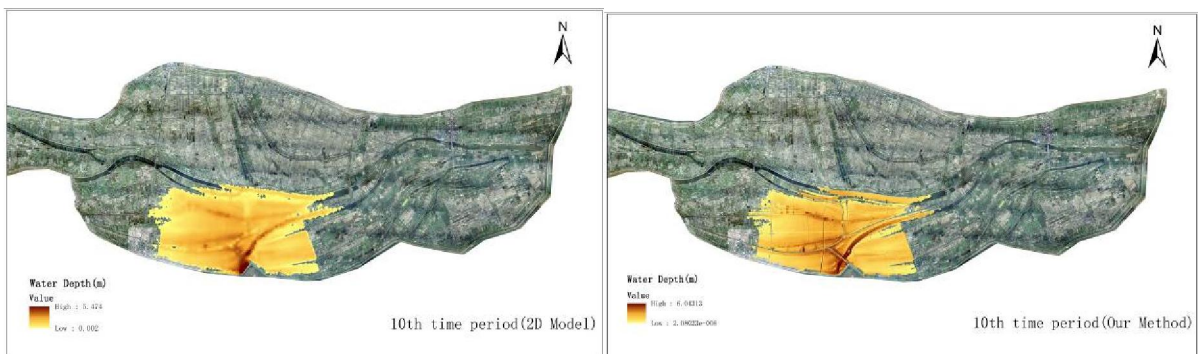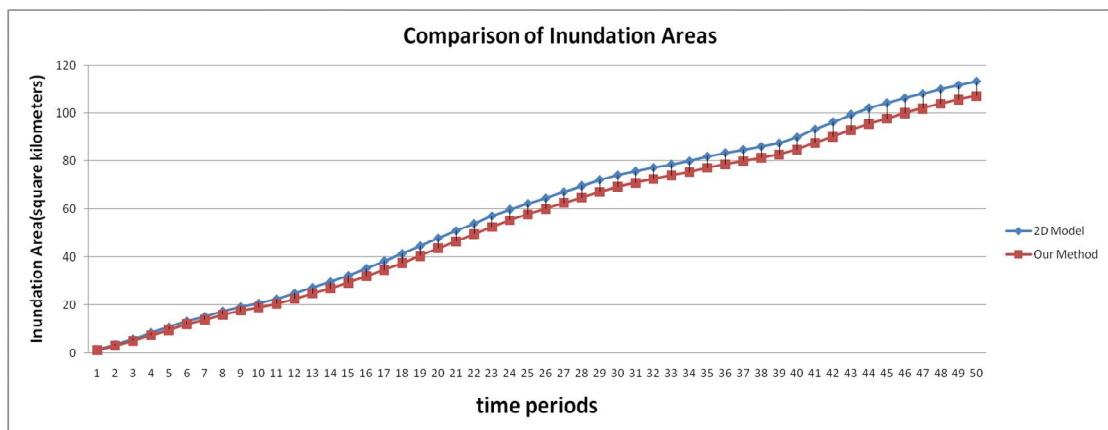

691

692
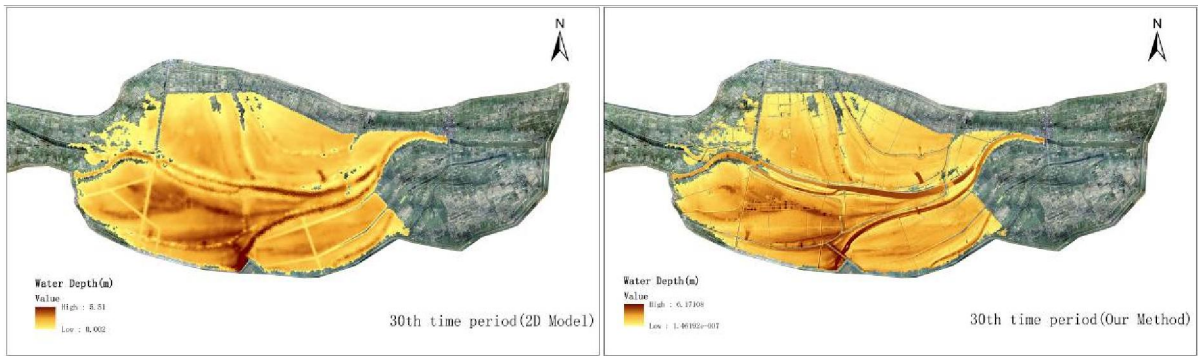
693

694 Figure 10 The Scheme of the inundation process of Gongshuangcha detention basin in three different time
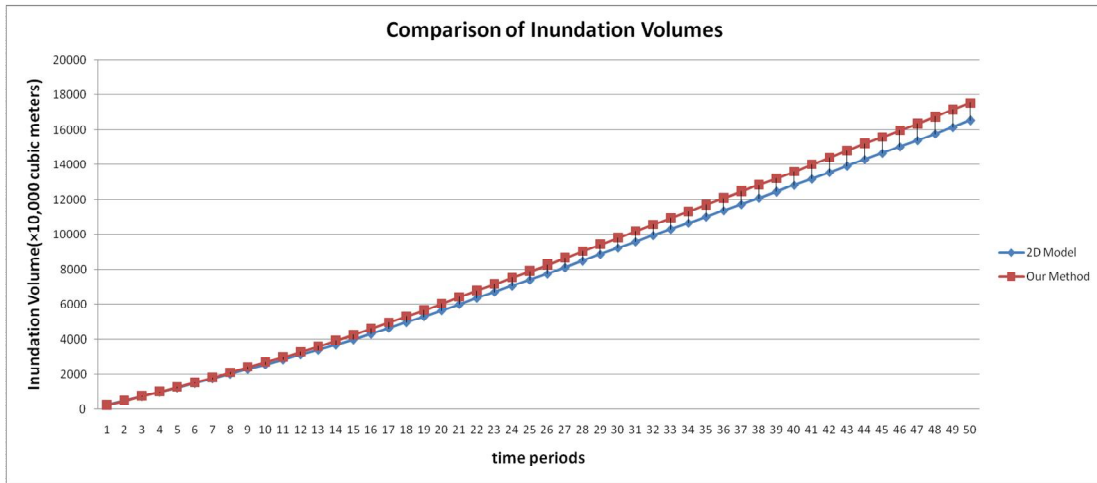
695 periods
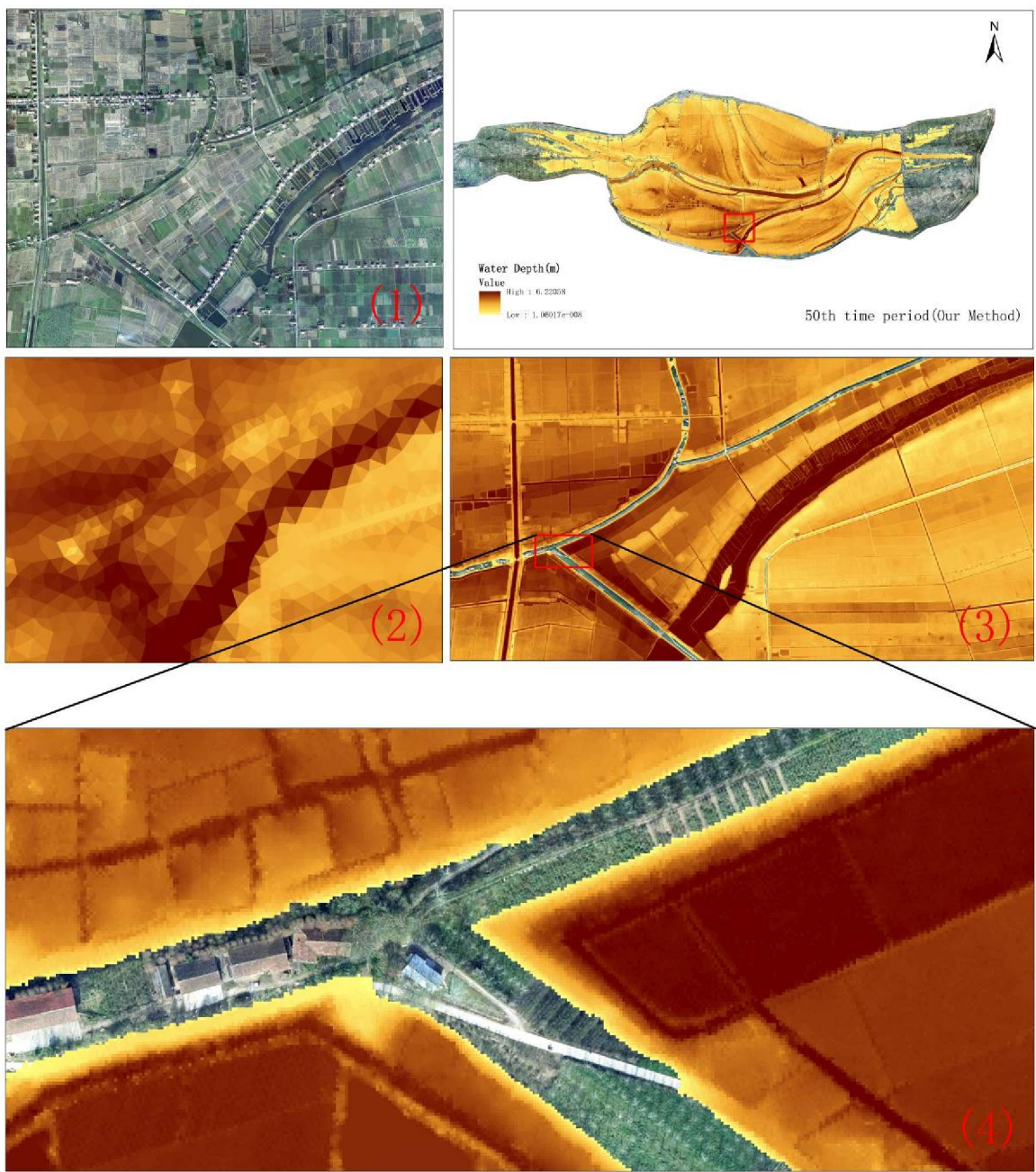
696

697   Figure 11 The scheme of the inundation process on the 50th time period and its regional enlarged view.

698

699   Figure 12 The Comparison of Inundation Areas in different time periods.

700

701   Figure 13 The Comparison of Inundation Volumes in different time periods.